Available online at www.sciencedirect.com
ScienceDirect
Journal of Computational Physics 227 (2008) 7264–7278
JOURNAL OF COMPUTATIONAL PHYSICS
www.elsevier.com/locate/jcp

An effective z-stretching method for paraxial light beam propagation simulations ☆

Leonel Gonzalez [a], Shekhar Guha [b], James W. Rogers [c,*], Qin Sheng [c]

[a] General Dynamics Information Technology, 5100 Springfield Street, Dayton, OH 45431, USA
[b] Materials and Manufacturing Directorate, Air Force Research Laboratory, 2977 Hobson Way, Wright Patterson AFB, OH 45433-7702, USA
[c] Center for Astrophysics, Space Physics; Engineering Research, Department of Mathematics, Baylor University, Waco, Texas 76798-7328, USA

Received 27 September 2007; received in revised form 31 March 2008; accepted 13 April 2008
Available online 30 April 2008

Abstract

A z-stretching finite difference method is developed for simulating the paraxial light beam propagation through a lens in a cylindrically symmetric domain. By introducing a domain transformation in the z-direction, we solve the corresponding complex difference equations containing an interface singularity over a computational space for great simplicity and efficiency. A specially designed matrix analysis is constructed to the study the numerical stability. Computational experiments are carried out for demonstrating our results.

MSC: 65M06; 65M50; 65Z05; 78A15; 78M20

Keywords: Light beam propagation; Interface singularity; Finite difference approximations; Domain transformation; Consistency; Stability; Uniform and nonuniform grids

1. Introduction

In order to reduce the computational complexity in light beam propagation simulations for practical applications, different types of approximation strategies are often necessary. In this article, we will take advantage of several known approximation procedures for paraxial optical waves to derive a highly efficient and robust numerical method that allows the application of conventional finite difference schemes on a uniform grid in the computational space, despite the difficulty of an interface presence in the physical domain.

☆ The third and fourth authors are supported in part by a research grant (No. AFGD-035-75CS) from the Air Force Research Laboratory and General Dynamics. The fourth author is also supported in part by the ASEE-SFFP Awards from the US Air Force.
* Corresponding author.
E-mail address: James_W_Rogers@baylor.edu (J.W. Rogers).

0021-9991/$ - see front matter © 2008 Elsevier Inc. All rights reserved.
doi:10.1016/j.jcp.2008.04.019

From Maxwell's field equations describing the behavior of monochromatic light, we may obtain the following time-dependent Helmholtz equation [2,6,7],

$$\nabla^2 E - \frac{1}{c^2}\frac{\partial^2 E}{\partial t^2} = 0, \tag{1.1}$$

where $E = E(x, y, z, t)$ is the electric field intensity, ∇^2 is the Laplacian operator, and c is the phase velocity, or speed of light in a particular medium.

Let E be the field intensity of a monochromatic plane wave of the form

$$E(x, y, z, t) = U(x, y, z)\mathrm{e}^{\mathrm{i}2\pi\nu t}, \quad \mathrm{i} = \sqrt{-1},$$

where ν is the frequency of the light. Then from (1.1) we acquire the time-independent Helmholtz equation

$$(\nabla^2 + \kappa^2)U(x, y, z) = 0, \tag{1.2}$$

where $\kappa = 2\pi\nu/c = 2\pi/\lambda$ is the *wave number*, and $\lambda = c/\nu$ is referred as the *wavelength*. Functions $|U(x, y, z)|$ and $\arg(U(x, y, z))$ are the *amplitude* and *phase of the wave*, respectively [6]. Assume that the z is the direction of the beam propagation. We may further consider the wave function with a complex amplitude, that is,

$$U(x, y, z) = u(x, y, z)\mathrm{e}^{-\mathrm{i}\kappa z}, \tag{1.3}$$

where u is referred as the *complex envelope*. A paraxial wave becomes realistic if the variation of u is slow in the z-direction.

Substitute (1.3) into (1.2) to yield

$$\nabla_{\mathrm{T}}^2 u(x, y, z) - 2\mathrm{i}k\frac{\partial u(x, y, z)}{\partial z} + \frac{\partial^2 u(x, y, z)}{\partial z^2} = 0, \tag{1.4}$$

where

$$\nabla_{\mathrm{T}}^2 = \frac{\partial^2}{\partial x^2} + \frac{\partial^2}{\partial y^2}$$

is the transverse Laplacian operator. In a paraxial case, we may assume that within a wavelength of the propagation distance, the change in u is sufficiently small compared to $|u|$ [17]. Thus,

$$\left|\frac{\partial^2 u}{\partial z^2}\right| \ll |\kappa^2 u|$$

which indicates that

$$\frac{\partial^2 u}{\partial z^2} \approx 0.$$

Therefore we arrive at an approximation of (1.4),

$$\nabla_{\mathrm{T}}^2 u(x, y, z) - 2\mathrm{i}\kappa\frac{\partial u(x, y, z)}{\partial z} = 0, \tag{1.5}$$

which is frequently called the *slowly varying envelope approximation of the Helmholtz equation* [1,7,18].

Under the polar transformation $r = \sqrt{x^2 + y^2}$ and $\phi = \arctan(y/x)$, (1.5) can be reformulated to

$$\left(\frac{1}{r}\frac{\partial}{\partial r} + \frac{\partial^2}{\partial r^2} + \frac{1}{r^2}\frac{\partial^2}{\partial \phi^2} - 2\mathrm{i}\kappa\frac{\partial}{\partial z}\right)u(r, z) = 0. \tag{1.6}$$

Eq. (1.6) has been utilized frequently in laser beam propagation modelings and computations in the past decades [7,8,21] (see Fig. 1.1).

Different finite difference, finite element schemes and the spectral method have been widely used in solving the Helmholtz equations including (1.4)–(1.6). The readers are referred to [2,7,14,21,22] and references therein for recent discussions in the area. While most of the frequently methods are successful, however, the industry continuously cries out for algorithmic simplicity, efficiency and reliability for targeted fast engineering

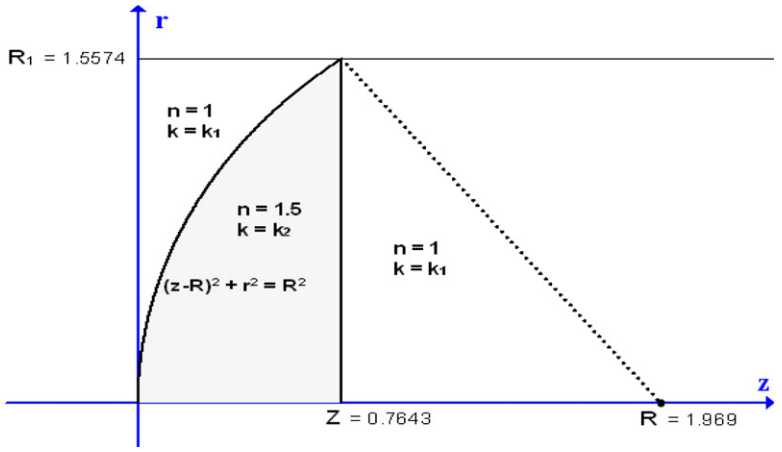

Fig. 1.1. A two-dimensional illustration of the interface of a cylindrically symmetric lens with a flat real surface [20]. We note that the top corner of the lens area will not cause any difficulty in paraxial computation cases.

simulations [8,16,20,21]. This motivates a different approach in our study. A typical cylindrically symmetric domain for spherical lens environments will be employed. For the situation we may assume [7] that

$$\frac{\partial^2 u}{\partial \phi^2} \equiv 0$$

and consequently, (1.6) can be simplified to yield the complex differential equation

$$2\mathrm{i}\kappa \frac{\partial u}{\partial z}(r,z) = \frac{\partial^2 u}{\partial r^2}(r,z) + \frac{1}{r}\frac{\partial u}{\partial r}(r,z), \quad 0 < r \leqslant \widetilde{R}_1 \leqslant R_1 \ll \infty. \tag{1.7}$$

We note that the coefficient of the first spacial derivative term in Eq. (1.7) becomes unbounded as $r \to 0$. The phenomenon is similar to the degeneracy singularity discussed in [4,19]. Although it will not affect the overall numerical stability and convergence of our difference scheme developed, and we may ease the unboundedness by multiplying both sides of the difference scheme by a scaling factor r in real computations, the singularity in (1.7) will lead to a stiff system of discretizations which requires a special attention from appropriate stiff solvers. We will leave this interesting issue to a forthcoming discussion. Further, based on our particular applications, we assume that the wavelength of light, λ, is 9.449 μm and that light is incident from air (refractive index $n_1 = 1$) into glen (refractive index $n_2 = 1.5$) so that we may adopt the following wave numbers in practical applications [7,20]

$$\kappa(r,z) = \begin{cases} \kappa_0 = \frac{2\pi n_1}{\lambda} \approx \frac{2}{3} \times 9.97543 \times 10^3 \text{ cm}^{-1}, & \text{in medium one;} \\ \kappa_1 = \frac{2\pi n_2}{\lambda} \approx 9.97543 \times 10^3 \text{ cm}^{-1}, & \text{in medium two.} \end{cases} \tag{1.8}$$

The above implies that a coefficient in (1.6), or (1.7), is discontinuous at the lens-interface. Relation (1.8) represents a single surface situation where the location of the interface is pre-determined. Although there have been a number of numerical methods for attacking the singular problem, many of them are relatively complicated for practical implementations [5,7,20,21]. It is therefore meaningful to introduce a simple, accurate and effective numerical method for straightforward computations in many engineering applications. Based on investigations of the single lens-interface cases, multiple interface scenarios can be discussed with additional κ values [20]. Needless to say, such multiple discontinuities will add a subsequent amount of complexities to the computation of the numerical solution [4,6,11,20].

Let us employ Neumann boundary conditions

$$u_r(z,0) = u_r(z,\widetilde{R}_1) = 0, \quad z > z_0, \tag{1.9}$$

at the bottom, $r = 0$ and top, $r = \widetilde{R}_1 \leqslant R_1$ of the physics domain [7,9,12].

For the initial condition of the differential equations (1.6), (1.7), we adopt the following standard approximation of a Gaussian beam with point source [1,5]

$$u(z_0,r)=\frac{A}{1+\mathrm{i}\vartheta}\exp\left(\mathrm{i}kz_0-\frac{r^2}{\beta^2(1+\mathrm{i}\vartheta)}\right), \tag{1.10}$$

where ϑ, β and A are parameters such that

$$\vartheta=\frac{2z_0}{\beta^2 k},\quad \frac{1}{\beta^2}=\frac{1}{\beta_0^2}+\frac{\mathrm{i}k}{2z_0},\quad A=\mathrm{e}^{\mathrm{i}kz_0},$$

and β_0 is the Gaussian beam width.

2. Base difference scheme and stability

Let $0\leqslant z\leqslant Z$ for (1.7)–(1.10). Further, let $h=R_1/M,\tau=Z/N$, where $M,N\in\mathbb{Z}^+$ are sufficiently large. We may introduce the uniform grid region,

$$\Omega_{h,\tau}=\{(mh,n\tau)|0\leqslant m\leqslant M,0\leqslant n\leqslant N\}$$

over the rectangular domain Ω used. For the sake of simplicity, we denote $r_m=mh,z_n=n\tau$ and $u_{m,n}=u(\tau_m,z_n)$. In addition, we will use $z_{n-\alpha},0<\alpha<1$, for specifying a non-grid point between z_{n-1} and z_n whenever needed.

Let us start with a linear second-order partial differential equation of the form

$$c_5\frac{\partial^2 u}{\partial z\partial r}+c_4\frac{\partial^2 u}{\partial r^2}+c_3\frac{\partial u}{\partial r}+c_2\frac{\partial u}{\partial z}+c_1u+c_0=0,\quad (r,z)\in\Omega, \tag{2.1}$$

together with (1.9), (1.10). The coefficients c_i of (2.1) are functions of z and r and may be discontinuous due to (1.8).

We propose a six-point, two-level Crank–Nicholson type scheme for solving 2.1 and (1.8)–(1.10),

$$\begin{aligned}&\frac{c_5}{2h\tau}[u_{m+1,n}-u_{m-1,n}-u_{m+1,n-1}+u_{m-1,n-1}]+\frac{c_4}{2h^2}[u_{m+1,n}-2u_{m,n}+u_{m-1,n}+u_{m+1,n-1}-2u_{m,n-1}+u_{m-1,n-1}]\\&\quad+\frac{c_3}{4h}[u_{m+1,n}-u_{m-1,n}+u_{m+1,n-1}-u_{m-1,n-1}]+\frac{c_2}{\tau}[u_{m,n}-u_{m,n-1}]+\frac{c_1}{2}[u_{m,n}+u_{m,n-1}]+c_0=0.\end{aligned}$$

The above can be conveniently reformulated to a partial difference equation

$$\begin{aligned}&\left(\frac{c_5}{2h\tau}+\frac{c_4}{2h^2}+\frac{c_3}{4h}\right)u_{m+1,n}+\left(-\frac{c_4}{h^2}+\frac{c_2}{\tau}+\frac{c_1}{2}\right)u_{m,n}+\left(-\frac{c_5}{2h\tau}+\frac{c_4}{2h^2}-\frac{c_3}{4h}\right)u_{m-1,n}\\&=\left(\frac{c_5}{2h\tau}-\frac{c_4}{2h^2}-\frac{c_3}{4h}\right)u_{m+1,n-1}+\left(\frac{c_4}{h^2}+\frac{c_2}{\tau}-\frac{c_1}{2}\right)u_{m,n-1}+\left(-\frac{c_5}{2h\tau}-\frac{c_4}{2h^2}+\frac{c_3}{4h}\right)u_{m-1,n-1}+c_0.\end{aligned} \tag{2.2}$$

Let w be a sufficiently smooth function defined on Ω. We define

$$Pw(r,z)=c_5\frac{\partial^2 w}{\partial z\partial r}+c_4\frac{\partial^2 w}{\partial r^2}(r,z)+c_3\frac{\partial w}{\partial r}(r,z)+c_2\frac{\partial w}{\partial z}(r,z)+c_1w(r,z)+c_0$$

and

$$\begin{aligned}P_{h,\tau}w_{m,n-1/2}=&\left(\frac{c_5}{2h\tau}+\frac{c_4}{2h^2}+\frac{c_3}{4h}\right)w_{m+1,n}+\left(-\frac{c_4}{h^2}+\frac{c_2}{\tau}+\frac{c_1}{2}\right)w_{m,n}+\left(-\frac{c_5}{2h\tau}+\frac{c_4}{2h^2}-\frac{c_3}{4h}\right)w_{m-1,n}\\&+\left(-\frac{c_5}{2h\tau}+\frac{c_4}{2h^2}+\frac{c_3}{4h}\right)w_{m+1,n-1}+\left(-\frac{c_4}{h^2}-\frac{c_2}{\tau}+\frac{c_1}{2}\right)w_{m,n-1}+\left(\frac{c_5}{2h\tau}+\frac{c_4}{2h^2}-\frac{c_3}{4h}\right)w_{m-1,n-1}+c_0.\end{aligned} \tag{2.3}$$

By expressing the function w at the grid points as Taylor expansions evaluated at reference point $\left(r_m,z_{n-\frac{1}{2}}\right)$ and substituting these into (2.3), it can be shown that

$$\|(P - P_{h,\tau})w_{m,n-1/2}\| = O(h^2 + h^2\tau^2 + \tau^2). \tag{2.4}$$

Let $\sigma = \tau/h$ be bounded and $\sigma \to 0$ as $h, \tau \to 0$. Then (2.4) ensures

1. the consistency of the finite difference scheme (2.2);
2. a second-order local truncation error of the scheme (2.2);
3. the numerical stability depends on the particular coefficients of the differential equation considered.

Definition 2.1. Consider a homogeneous finite difference scheme written as a system of linear equations as below:

$$B\mathbf{u}_n = C\mathbf{u}_{n-1}$$

or

$$\mathbf{u}_n = B^{-1}C\mathbf{u}_{n-1}$$

where vector $\mathbf{u}_n = \{u_{k,n}\}_{k=0}^{M}$ and the difference operators $B, C \in \mathbb{C}^{M\times M}$ are coefficient matrices. Let $E = B^{-1}C$. If there exists a constant $K > 0$ independent of n, h and τ such that $\|E^n\| \leqslant K$ for some norm $\|\cdot\|$, we say that the scheme is stable in the Lax–Richtmyer sense [13,15].

Due to the inclusion of a cross-derivative term in our transformed equation, our difference scheme will not be stable in the Lax–Richtmyer sense. We define a notion of practical stability which holds for a range of propagation step sizes that afford us sufficient resolution in our simulations.

Definition 2.2. Let $\rho(B^{-1}C)$ be the spectral radius of kernel matrix $B^{-1}C$. If

$$\rho(B^{-1}C) \leqslant 1$$

at all propagation steps $0 < n\tau < T$ with a transverse direction step size $\epsilon_0 < h < \epsilon_1$ for some $\epsilon_1 > \epsilon_0 > 0$, we say that the scheme

$$B\mathbf{u}_n = C\mathbf{u}_{n-1}$$

is stable within a parameter range.

While this stability condition does not specify a norm for convergence, it does guarantee that perturbations will not increase exponentially with n.

Definition 2.3. A matrix $A \in \mathbb{C}^{n\times n}$ is said to be positive semistable if every eigenvalue of A has nonnegative real part.

Theorem 2.4. *Let $A, B, C, G \in \mathbb{C}^{M\times M}$ be such that*

$$B = G + A, \quad C = G - A.$$

Then the difference scheme defined by

$$B\mathbf{u}_n = C\mathbf{u}_{n-1}$$

is stable if and only if $G^{-1}A$ is positive semistable.

Corollary 2.5. *Let $A, B, C \in \mathbb{C}^{M\times M}$, d be a positive real number such that*

$$B = dI + A, \quad C = dI - A.$$

Then the difference scheme defined by

$$B\mathbf{u}_n = C\mathbf{u}_{n-1}$$

is stable if and only if A is positive semistable.

Recall (1.7). We have the corresponding paraxial Helmholtz coefficients for the general Eqs. (2.1) and (2.2),

$$c_5 = 0, \quad c_4 = 1, \quad c_3 = \frac{1}{r}, \quad c_2 = -2i\kappa, \quad c_1 = 0, \quad c_0 = 0. \tag{2.5}$$

It follows therefore that (2.2), (1.9) and (1.10) can be simplified to the following homogeneous paraxial Helmholtz difference scheme,

$$-\alpha\left(1+\frac{1}{2m}\right)u_{m+1,n}+(2+2\alpha)u_{m,n}-\alpha\left(1-\frac{1}{2m}\right)u_{m-1,n}$$
$$=\alpha\left(1+\frac{1}{2m}\right)u_{m+1,n-1}+(2-2\alpha)u_{m,n-1}+\alpha\left(1-\frac{1}{2m}\right)u_{m-1,n-1}, \tag{2.6}$$

$$u_{m,0}=\mathrm{e}^{-hm/\beta_0}, \tag{2.7}$$

$$-2\alpha u_{1,n}+(2+2\alpha)u_{0,n}=2\alpha u_{1,n-1}+(2-2\alpha)u_{0,n-1}, \tag{2.8}$$

$$(2+2\alpha)u_{M,n}-2\alpha u_{M-1,n}=(2-2\alpha)u_{M,n-1}+2\alpha u_{M-1,n-1}, \tag{2.9}$$

where

$$\alpha=-\frac{\tau\mathrm{i}}{2\kappa h^2}.$$

Following the analysis method outlined above, we can express our scheme in matrix form

$$B\mathbf{u}_n=C\mathbf{u}_{n-1}$$

where $B=G+A, C=G-A, G=2I$, and A is tridiagonal. Investigating properties of the eigenvalues of $A=\{a_{m,n}\}$, where

$$a_{m,m}=2\alpha,\quad m=0,1,\ldots,M,$$

$$a_{m,m-1}=-\alpha\left(1-\frac{1}{2m}\right),\quad m=1,2,\ldots,M-1,$$

$$a_{M,M-1}=-2\alpha,$$

$$a_{m,m+1}=-\alpha\left(1+\frac{1}{2m}\right),\quad m=1,2,\ldots,M-1,$$

$$a_{0,1}=-2\alpha,$$

we are able to show that the eigenvalues of matrix A are purely imaginary, and thus have nonnegative real parts. Thus, A is positive semidefinite. By Corollary 2.5, we can show the following.

Theorem 2.6. *Let κ be a constant. Then the homogeneous paraxial Helmholtz difference scheme (2.6)–(2.9) is stable. Further, there is lower boundary restriction on the step size parameter, h, in this case.*

3. z-stretching domain transformation

One possible way of avoiding the computational difficulties presented by the discontinuity of κ at the interface is by decomposing the domain into three sections, pre-lens, lens, and post-lens, and *stretching* each segment by one-to-one transformations onto rectangular areas. We would then be able to use conventional finite difference techniques, such as that introduced in Section 2, to solve (2.1) together with initial-boundary conditions on each segment. The grid stretch can be achieved either in the direction of electro-magnetic wave propagation z, or the direction of r. Each of the approaches have distinct advantages. We will only focus on the former strategy in this paper. In this case, the numerical solution computed at the rightmost edge of the pre-lens segment becomes the initial condition of the next segment.

Let $r=r(\xi,\zeta), z=z(\xi,\zeta)$ be the one-to-one stretching transformation to be used. Thus,

$$\frac{\partial u}{\partial r}=\frac{\partial u}{\partial \xi}\frac{\partial \xi}{\partial r}+\frac{\partial u}{\partial \zeta}\frac{\partial \zeta}{\partial r},\quad \frac{\partial u}{\partial z}=\frac{\partial u}{\partial \xi}\frac{\partial \xi}{\partial z}+\frac{\partial u}{\partial \zeta}\frac{\partial \zeta}{\partial z},$$

$$\frac{\partial^2 u}{\partial r^2}=\frac{\partial u}{\partial \xi}\frac{\partial^2 \xi}{\partial r^2}+\frac{\partial^2 u}{\partial \xi^2}\left(\frac{\partial \xi}{\partial r}\right)^2+2\frac{\partial^2 u}{\partial \xi\partial \zeta}\frac{\partial \xi}{\partial r}\frac{\partial \zeta}{\partial r}+\frac{\partial u}{\partial \zeta}\frac{\partial^2 \zeta}{\partial r^2}+\frac{\partial^2 u}{\partial \zeta^2}\left(\frac{\partial \zeta}{\partial r}\right)^2.$$

A substitution of the above into (1.7) yields

$$2i\kappa\left(\frac{\partial u}{\partial \xi}\frac{\partial \xi}{\partial z}+\frac{\partial u}{\partial \zeta}\frac{\partial \zeta}{\partial z}\right)=\frac{\partial u}{\partial \xi}\frac{\partial^2 \xi}{\partial r^2}+\frac{\partial^2 u}{\partial \xi^2}\left(\frac{\partial \xi}{\partial r}\right)^2+2\frac{\partial^2 u}{\partial \xi \partial \zeta}\frac{\partial \xi}{\partial r}\frac{\partial \zeta}{\partial r}+\frac{\partial u}{\partial \zeta}\frac{\partial^2 \zeta}{\partial r^2}+\frac{\partial^2 u}{\partial \zeta^2}\left(\frac{\partial \zeta}{\partial r}\right)^2+\frac{1}{r}\left(\frac{\partial u}{\partial \xi}\frac{\partial \xi}{\partial r}+\frac{\partial u}{\partial \zeta}\frac{\partial \zeta}{\partial r}\right),$$

which can be regrouped into

$$\left(2i\kappa\frac{\partial \zeta}{\partial z}-\frac{\partial^2 \zeta}{\partial r^2}-\frac{1}{r}\frac{\partial \zeta}{\partial r}\right)\frac{\partial u}{\partial \zeta}=\left(-2i\kappa\frac{\partial \xi}{\partial z}+\frac{\partial^2 \xi}{\partial r^2}+\frac{1}{r}\frac{\partial \xi}{\partial r}\right)\frac{\partial u}{\partial \xi}+\left(\frac{\partial \xi}{\partial r}\right)^2\frac{\partial^2 u}{\partial \xi^2}+2\left(\frac{\partial \xi}{\partial r}\frac{\partial \zeta}{\partial r}\right)\frac{\partial^2 u}{\partial \xi \partial \zeta}+\left(\frac{\partial \zeta}{\partial r}\right)^2\frac{\partial^2 u}{\partial \zeta^2}. \tag{3.1}$$

To map the lens area $\Omega=\{0\leqslant z\leqslant Z,(z-R)^2+r^2\leqslant R^2,r\geqslant 0\}$ into a rectangular area $\widetilde{\Omega}=\{0\leqslant\zeta\leqslant Z,\ 0\leqslant\xi\leqslant R_1\}$, a natural choice is the following transformation,

$$\xi(r,z)=r,\quad \zeta(r,z)=\frac{z-R+\sqrt{R^2-r^2}}{Z-R+\sqrt{R^2-r^2}}Z.$$

In this particular case we have

$$\frac{\partial \xi}{\partial r}=1,\quad \frac{\partial \xi}{\partial z}=0,\quad \frac{\partial^2 \xi}{\partial r^2}=0,$$
$$\frac{\partial \zeta}{\partial r}=\frac{rZ(z-Z)}{\rho^2\sqrt{R^2-r^2}},\quad \frac{\partial \zeta}{\partial z}=\frac{Z}{\rho},\quad \frac{\partial^2 \zeta}{\partial r^2}=\frac{Z(z-Z)(\rho R^2+2r^2\sqrt{R^2-r^2})}{\rho^3(R^2-r^2)^{3/2}},$$

where $\rho=Z-R+\sqrt{R^2-r^2}$. We define functions

$$\phi(\xi,\zeta):=\frac{\partial \zeta}{\partial r}(r(\xi,\zeta),z(\xi,\zeta))=\frac{(\zeta-Z)\xi}{\sqrt{R^2-\xi^2}[Z-(R-\sqrt{R^2-\xi^2})]},$$
$$\psi(\xi,\zeta):=\frac{\partial^2 \zeta}{\partial r^2}(r(\xi,\zeta),z(\xi,\zeta))=\frac{(\zeta-Z)[R^3-\sqrt{R^2-\xi^2}(R^2+2\xi^2)-Z]}{(R^2-\xi^2)^{\frac{3}{2}}[Z-(R-\sqrt{R^2-\xi^2})]^2},$$
$$\theta(\xi,\zeta):=\frac{\partial \zeta}{\partial z}(r(\xi,\zeta),z(\xi,\zeta))=\frac{Z}{Z-(R-\sqrt{R^2-\xi^2})}.$$

Subsequently, (3.1) can be simplified to

$$\left(2i\kappa\theta-\psi-\frac{1}{\xi}\phi\right)\frac{\partial u}{\partial \zeta}=\frac{1}{\xi}\frac{\partial u}{\partial \xi}+\frac{\partial^2 u}{\partial \xi^2}+2\phi\frac{\partial^2 u}{\partial \xi \partial \zeta}+\phi^2\frac{\partial^2 u}{\partial \zeta^2}. \tag{3.2}$$

It can be demonstrated that at every point in the transformed lens segment, we have

$$\phi^2\left|\frac{\partial^2 u}{\partial \zeta^2}\right|\leqslant\frac{R_1^2 Z}{(R^2-R_1^2)\left[Z-\left(R-\sqrt{R^2-R_1^2}\right)\right]}\left|\frac{\partial^2 u}{\partial z^2}\right|\approx 0.$$

Thus, for a typical lens where the slowly varying envelope approximation is applicable, (3.2) can be simplified to a more appropriate form for computations within the transformed lens area,

$$\left(2i\kappa\theta-\psi-\frac{1}{\xi}\phi\right)\frac{\partial u}{\partial \zeta}=\frac{1}{\xi}\frac{\partial u}{\partial \xi}+\frac{\partial^2 u}{\partial \xi^2}+2\phi\frac{\partial^2 u}{\partial \xi \partial \zeta},\quad \xi>0. \tag{3.3}$$

Again, we notice that the function $1/\xi$ becomes unbounded if ξ is arbitrarily small. This may indicate a considerably strong stiffness of the system of linear equations generated via z-stretching type of discretizations if the spacial step is chosen to be small.

In Fig. 3.1, we illustrate the z-stretching by showing an example of the grid within the lens before and after the stretching. It is evident that the transformation enables the six-point scheme to work accurately and efficiently. Instead of (2.5), now we have the following set of adjusted coefficients for the in-lens segment difference scheme,

$$c_5 = 2\phi, \quad c_4 = 1, \quad c_3 = \frac{1}{\xi}, \quad c_2 = -2i\kappa\theta + \psi + \frac{1}{\xi}\phi, \quad c_1 = 0, \quad c_0 = 0.$$

Subsequently, (2.6) can be modified to

$$\begin{aligned} &-\gamma\left[\frac{2\phi}{h} + \alpha\left(1 + \frac{1}{2m}\right)\right]u_{m+1,n} + (2 + 2\alpha\gamma)u_{m,n} - \gamma\left[-\frac{2\phi}{h} + \alpha\left(1 - \frac{1}{2m}\right)\right]u_{m-1,n} \\ &\quad = \gamma\left[-\frac{2\phi}{h} + \alpha\left(1 + \frac{1}{2m}\right)\right]u_{m+1,n-1} + (2 - 2\alpha\gamma)u_{m,n-1} + \gamma\left[\frac{2\phi}{h} + \alpha\left(1 - \frac{1}{2m}\right)\right]u_{m-1,n-1}, \end{aligned} \tag{3.4}$$

where

$$\alpha = \frac{\tau}{h^2} \quad \text{and} \quad \gamma = \gamma(\xi,\zeta) = \left(2i\kappa\theta - \psi - \frac{1}{\xi}\phi\right)^{-1}. \tag{3.5}$$

In this method, the Gaussian beam input equation is evaluated at the lens surface, and becomes the initial solution of the simulation at the edge of the lens segment. No computation is necessary in the pre-lens segment. The solution at the right edge of the lens segment becomes the initial solution of the post-lens segment, which we simulate using the homogeneous scheme described earlier. To reduce the unboundedness of the coefficients due to the step size h, we may scaling (3.4) by multiplying both sides of the equations by h. This will not change the stiffness of the linear system obtained, but it does improve the numerical computations significantly, as far as an appropriate stiff solver is employed.

To determine the boundary conditions applicable within the lens segment, note that

$$\frac{\partial u}{\partial r}(\xi,\zeta) = \frac{\partial u}{\partial \xi}(\xi,\zeta)\frac{\partial \xi}{\partial r}(\xi,\zeta) + \frac{\partial u}{\partial \zeta}(\xi,\zeta)\frac{\partial \zeta}{\partial r}(\xi,\zeta),$$

thus

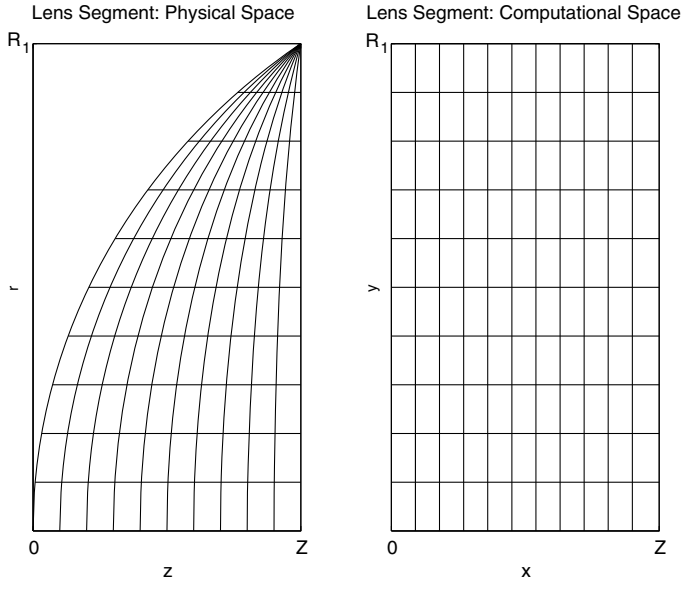

Fig. 3.1. Left: An in-lens domain before a z-stretching. Right: The in-lens domain after a z-stretching.

$$\frac{\partial u}{\partial \xi}(0,\zeta) = \frac{\partial u}{\partial \xi}(\widetilde{R}_1,\zeta) = 0, \quad 0 < \zeta < Z. \tag{3.6}$$

It is interesting to note that for a lens that tapers to a point at the top, the geometric interpretation of this new boundary condition is that the single point $(\widetilde{R}_1, Z)$ has been stretched into the upper edge of our transformed rectangular domain, i.e. the upper boundary in the computational space corresponds to the single point $(\widetilde{R}_1, Z)$ in the physical space.

To demonstrate stability, we use the matrix analysis method introduced in the previous section. For our scheme $B\mathbf{u}_n = C\mathbf{u}_{n-1}$, we have $B = G + A, C = G - A$ with matrix $G = \{g_{m,n}\}$ and $A = \{a_{m,n}\}$, where

$$\begin{aligned}
&g_{m,m} = 2, \quad m = 0,1,\ldots,M,\\
&g_{m,m-1} = \frac{2\gamma\phi}{h}, \quad m = 1,2,\ldots,M-1,\\
&g_{M,M-1} = 0,\\
&g_{m,m+1} = \frac{-2\gamma\phi}{h}, \quad m = 1,2,\ldots,M-1,\\
&g_{0,1} = 0,
\end{aligned}$$

$$\begin{aligned}
&a_{m,m} = 2\alpha\gamma, \quad m = 0,1,\ldots,M,\\
&a_{m,m-1} = -\alpha\gamma\left(1 - \frac{1}{2m}\right), \quad m = 1,2,\ldots,M-1,\\
&a_{M,M-1} = -2\alpha\gamma,\\
&a_{m,m+1} = -\alpha\gamma\left(1 + \frac{1}{2m}\right), \quad m = 1,2,\ldots,M-1,\\
&a_{0,1} = -2\alpha\gamma.
\end{aligned}$$

Examining the real part of function $\gamma(\xi,\zeta)$ resulting from our chosen transformation, we see that matrix A is positive semistable. This property will still hold if the transformation is adapted to other convex lens shapes. If we have a transverse step size h such that

$$h > 2\tau|\gamma(\xi,\zeta)\phi(\xi,\zeta)| \text{ for } 0 \leqslant \xi \leqslant R_1, \quad 0 \leqslant \zeta \leqslant Z,$$

or equivalently, if the number of grid points in the ξ direction, M, is such that

$$M < \frac{R_1}{h_{\min}}$$

where

$$h_{\min} = 2\tau \max_{\xi,\zeta} |\gamma(\xi,\zeta)\phi(\xi,\zeta)|$$

then matrix $G + G^*$ is positive definite. Then based on Theorem 2.4, we can prove the following.

Theorem 3.1. *Let κ be discontinuous as given by (1.8) and*

$$h > 2\tau|\gamma(\xi,\zeta)\phi(\xi,\zeta)| \quad \text{for} \quad 0 < \xi \leqslant \widetilde{R}_1, \quad 0 < \zeta \leqslant Z.$$

Then the difference scheme (3.4)–(3.6) is stable on z-stretched domains.

The theorem posts a restriction on the value of τ/h, though this condition is relatively easy to satisfy. For the parameter values utilized in our simulations,

$$\kappa = 9.97543 \times 10^3, \quad R = 1.969, \quad Z = 0.7643, \quad R_1 = \widetilde{R}_1 = 1.5574, \tag{3.7}$$

Table 3.1
Maximum grid points in the transverse direction with $R = 1$

Z	$k = 8000$	$k = 10000$	$k = 12000$
0.1	7439	9365	11279
0.3	5642	7046	8848
0.5	4059	5064	6068
0.7	2496	3104	3711
0.9	1033	1257	1479

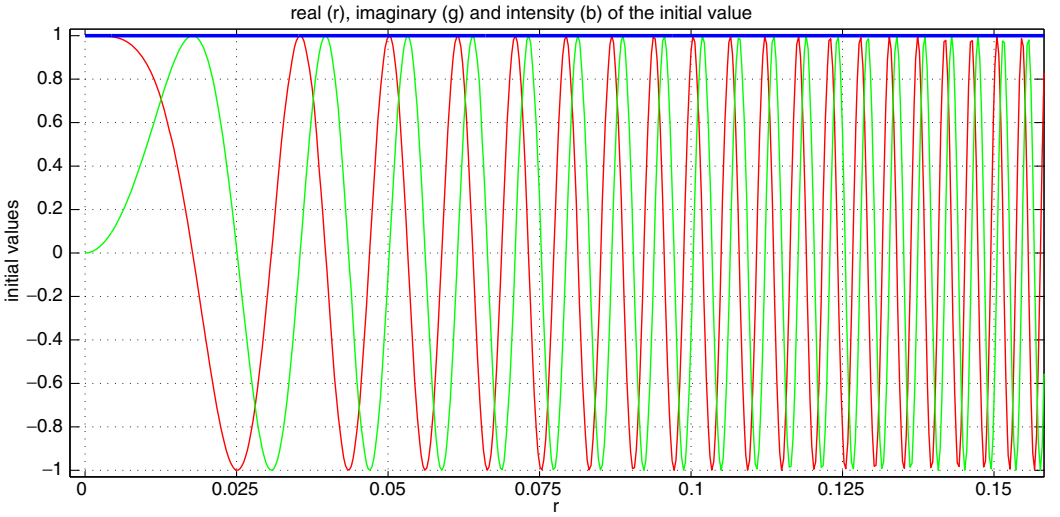

Fig. 4.1. Normalized initial value function $u(r, 0)$. Red (or dark colored) curve is for the real part and green (or light colored) curve is for the imaginary part of the function. Highly oscillatory features of the function is clear. (For interpretation of the references to colour in this figure legend, the reader is referred to the web version of this article.)

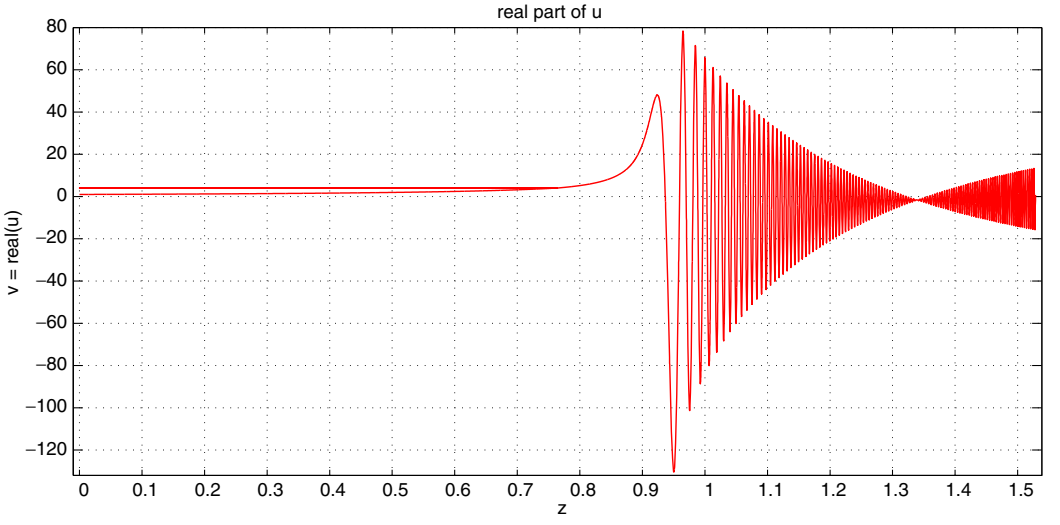

Fig. 4.2. Real part of the simulated solution at the center point $r = 0$. The numerical solution increases rapidly as z approaches the focusing location. Then the simulated oscillatory wave diffuses after the focusing point.

we need $M \leqslant 1.2092 \times 10^4$. We list a sampling of maximum grid points M for other parameter values (see Table 3.1).

4. Simulation results and observations

All simulated results were implemented on dual processor DELL workstations with at least double precision. MATLAB, FORTRAN and C++ programming languages were utilized. Dimensionless models are used throughout the computations. For the sake of simplicity, we do not tend to re-scale numerical solutions back to their original physical dimensions in simulations (see Fig. 4.1).

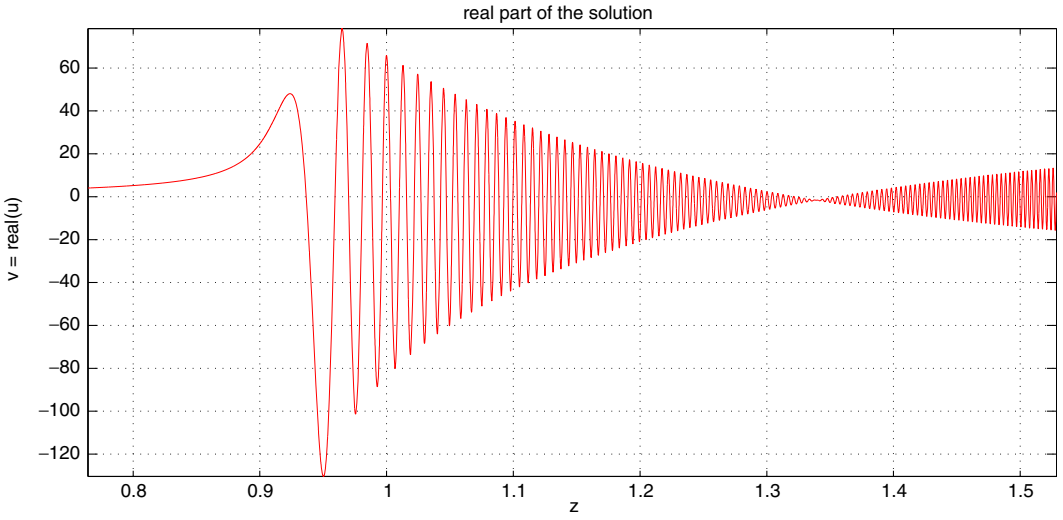

Fig. 4.3. More detailed real part of the simulated solution near the focus point, $r = 0$. Same conditions as in Fig. 4.2 are used.

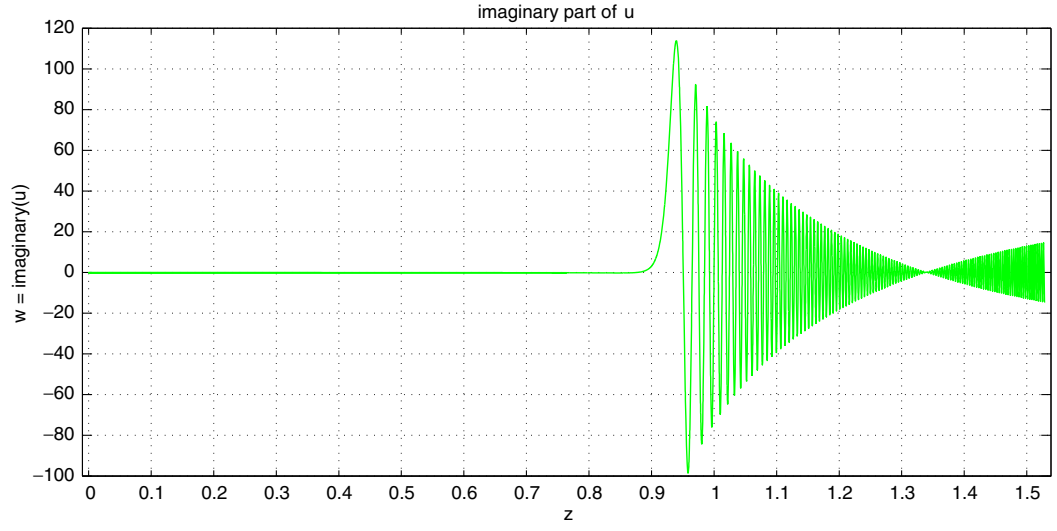

Fig. 4.4. Imaginary part of the simulated solution at the center point $r = 0$. The numerical solution increases rapidly as z approaches the focusing location. Then the simulated oscillatory wave diffuses after the focusing point.

In the following numerical experiments we use parameters (3.7) listed in the previous section. We further select $h = R_1/M$ where $M = 5 \times 10^3$ and $\tau = Z/N$ where $N = 1.6 \times 10^4$ in the six-point scheme used in the computational solution space after a designated z-stretching.

We show the real part of the simulated solution, $a(z) = \text{real}\{u(0,z)\}$, in Figs. 4.2 and 4.3. We may observe that while the function value of a is relatively stable before the focusing point $z_f \approx 0.94778$, it increases dramatically as $z \to z_f$. This can be viewed more precisely in the enlarged picture of Fig. 4.3.

Figs 4.4 and 4.5 are devoted to the imaginary part of the numerical solution, $b(z) = \text{imaginary}\{u(0,z)\}$. Similar to the real part, b is relatively stable before the focusing point $z_f \approx 2.7431$ and is highly oscillatory as $z \to z_f$. The phenomenon can be viewed more clearly in the enlarged picture of Fig. 4.5.

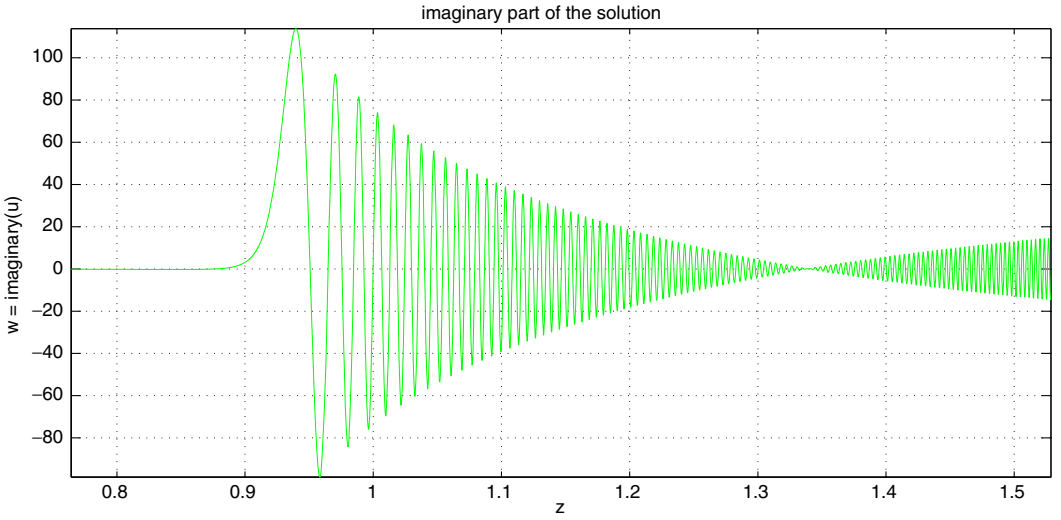

Fig. 4.5. More detailed imaginary part of the simulated solution near the focus point, $r = 0$. Same conditions as in Fig. 4.4 are used.

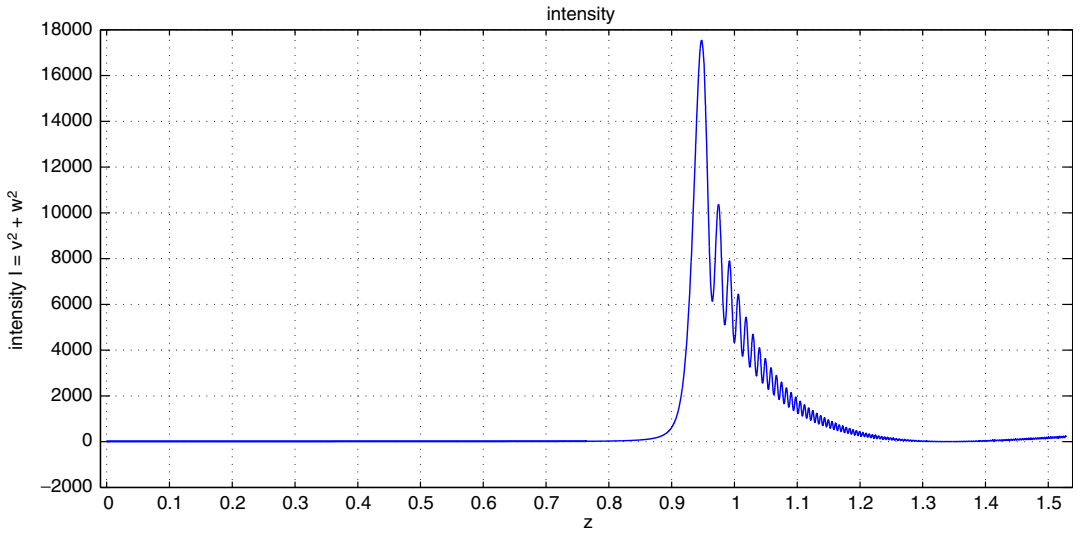

Fig. 4.6. Numerical intensity function of the simulated solution at the center point $r = 0$. The intensity increases rapidly as z approaches the focusing location. Then the intensity value diffuses out after the focusing point.

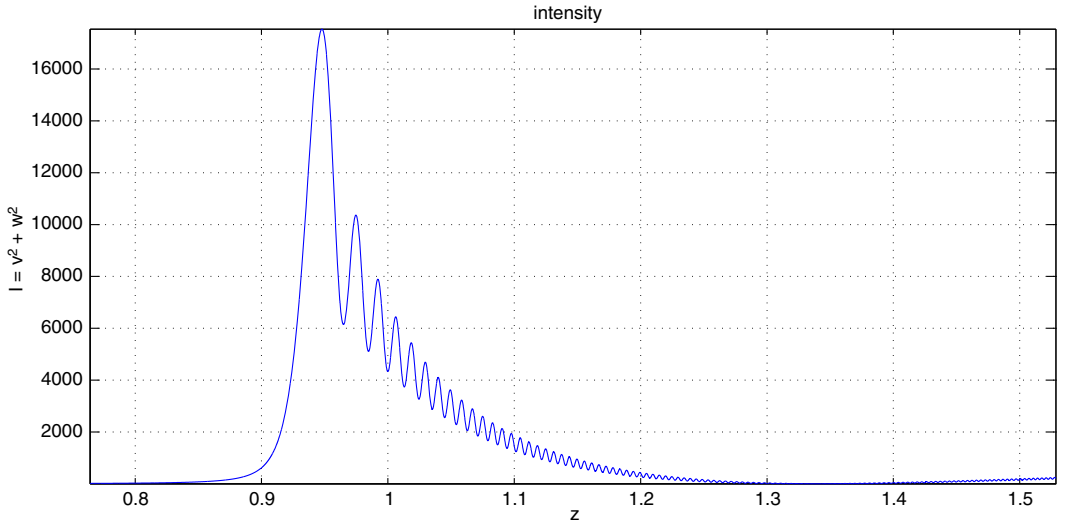

Fig. 4.7. More detailed numerical intensity function of the simulated solution near the focus point ($r = 0$). Same conditions as in Fig. 4.6 are used.

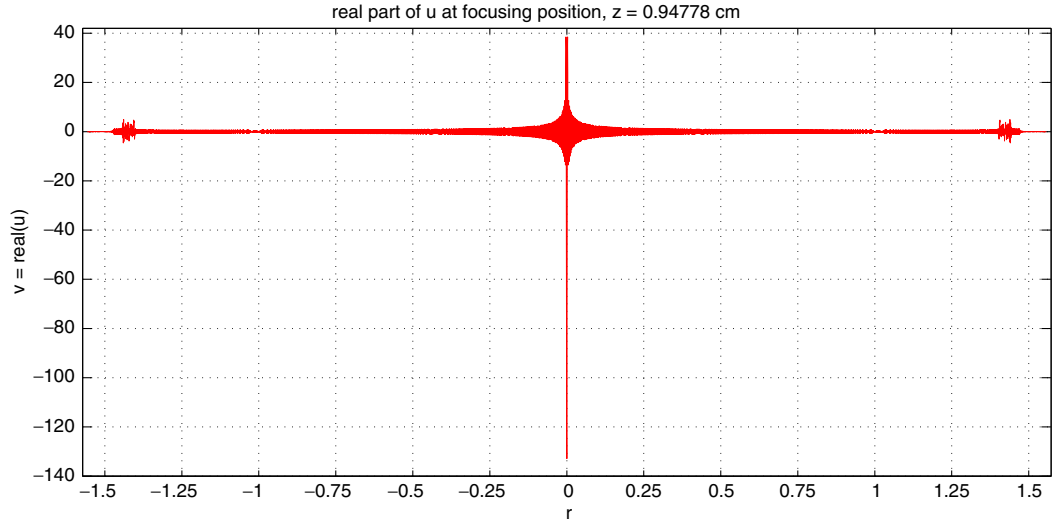

Fig. 4.8. Highly oscillatory numerical intensity function of the simulated solution at the focusing location $z = 2.7431$. The computed intensity increases exponentially near the center, as compared with much lower profiles away from the focusing area.

Define the *numerical intensity function* as

$$\mathcal{T}(r,z) = \sqrt{\text{real}^2[u(r,z)] + \text{imag}^2[u(r,z)]} \geqslant 0, \quad 0 \leqslant r \leqslant R_1, \quad 0 \leqslant z \leqslant Z. \tag{4.1}$$

In Figs. 4.6 and 4.7 we plot this intensity function against the propagation direction z as r being chosen as zero. It is interesting to find that the intensity increases rapidly as $z \to z_f$. The observation is consistent with our previous results.

As a comparison, we further plot the numerical intensity function at the locations near and at the focusing point in Figs 4.8 and 4.9. It is observed that the numerical estimate of the intensity oscillates rapidly in the r-direction. The intensity increases sharply near the center point of the lens, $r = 0$, while z approaches the

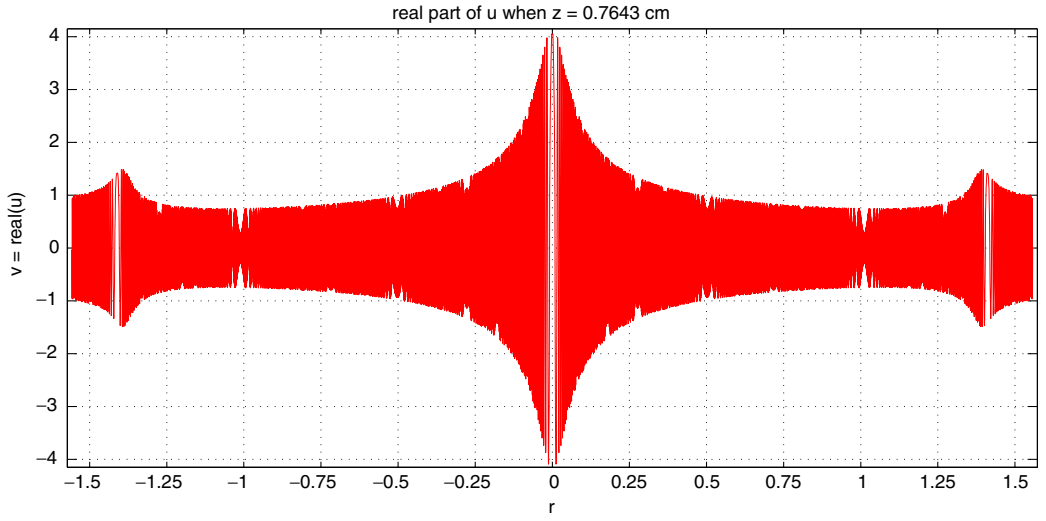

Fig. 4.9. Details of the highly oscillatory numerical intensity function of the simulated solution at $z = 0.7643$. The intensity builds up near the center of the lens at $r = 0$.

focusing point location. The simulated wave profiles well match the experimental results. The algorithms can be used to provide reference values for further explorations.

5. Conclusions and remarks

In this investigation, we have developed a *z-stretching domain transformation* to map the lens and post-lens domains into convenient rectangular shapes, where we can utilize well established finite difference methods on uniform grids. The resulting method provides a useful approximation technique that can be efficiently implemented with less than 50 lines of Matlab code in the simulation loops. This simplicity is extremely useful in fast engineering computations and simulations. Although a stiff system solver is needed, this does not add extra inconvenience due to many commonly available programming packages. The stretching schemes have demonstrated extremely stable and accurate in computational experiments, and the solutions obtained have met well physical expectations.

A more powerful strategy may be the use of optimally combined z and r stretching transformations to increase computational resolution and accuracy of the numerical solution in critical local regions. Magnifying a particular subregion in the transformed coordinate space is computationally equivalent to increasing the refinement of the grid in that region using techniques such as adaptive mesh refinement [3,19] and scattering [16]. Alternatively, domain transformation could facilitate the use of established adaptive grid techniques, since applications of standard mesh refinement or moving mesh technics are straightforward on rectangular domains [10,19]. The technique may also provide an effective way for solving problems in which locations of interfaces are not pre-determined. More precise studies on degeneracy singularities have also been carried out and have made excellent progress. Further, hyperbolic smoothness maps have also been proved to be extremely useful auxiliary tools to consider in practical optical beam and acoustic computations [20,22]. Detailed discussions will be given in our forthcoming reports.

Acknowledgments

The third and fourth authors would like to thank the United States Air Force Research Laboratory for the generous support through the Grant of No. AFGD-035-75CS and the ASEE-SFFP Awards. The authors would like also to thank the referees sincerely for enthusiastic suggestions which helped to improve the contents of this article.

References

[1] Y.B. Band, Light and Matter: Electromagnetism, Optics, Spectroscopy and Lasers, John Wiley & Sons, West Sussex, 2006.
[2] G. Bao, G.W. Wei, S. Zhao, Numerical solution of the Helmholtz equation with high wavenumbers, Int. J. Numer. Meth. Eng. 59 (2004) 389–408.
[3] M. Berger, J. Oliger, Adaptive mesh refinement for hyperbolic partial differential equations, J. Comp. Phys. 53 (1984) 484–512.
[4] H. Cheng, P. Lin, Q. Sheng, R. Tan, Solving degenerate reaction–diffusion equations via variable step Peaceman–Rachford splitting, SIAM J. Sci. Comput. 25 (2003) 1273–1292.
[5] H.J. Eom, Electromagnetic Wave Theory for Boundary-Value Problems – An Advanced Course on Analytical Methods, Springer-Verlag, Berlin Heidelberg, 2004.
[6] J.W. Goodman, Introduction to Fourier Optics, third ed., Roberts & Company Publishers, Denver, 2004.
[7] S. Guha, Validity of the paraxial approximation in the focal region of a small-f-number lens, Opt. Lett. 26 (2001) 1598–1600.
[8] S. Guha, G.D. Gillen, Description of light propagation through a circular aperture using non-paraxial vector diffraction theory, Opt. Express 13 (2005) 1424–1447.
[9] P. Joly, J.-R. Li, S. Fliss, Exact boundary conditions for periodic waveguides containing a local perturbation, Commun. Comput. Phys. 1 (2006) 945–973.
[10] I.S. Kim, W.J.R. Hoefer, A local mesh refinement algorithm for the time domain-finite difference method using Maxwell's equations, IEEE Trans. Microwave Theory Tech. 38 (1990) 812–815.
[11] E. Larsson, A domain decomposition method for the Helmholtz equation in a multilayer domain, SIAM J. Sci. Comput. 20 (1999) 1713–1731.
[12] M. de Laurentis, A. Irace, G. Breglio, Determination of single mode condition in dielectric rib waveguide with large cross section by finite element analysis, J. Comput. Electron. 6 (2007) 285–287.
[13] P.D. Lax, R.D. Richtmeyer, Survey of the stability of linear finite difference equations, Commun. Pure Appl. Math. 9 (1956) 267–294.
[14] Y.Y. Lu, Some techniques for computing wave propagation in optical waveguides, Commun. Comput. Phys. 1 (2006) 1056–1075.
[15] K.W. Morton, Stability of finite difference approximations to a diffusion–convection equation, Int. J. Num. Meth. Eng. 15 (1980) 677–683.
[16] D.P. Nicholls, F. Reitich, Shape deformations in rough surface scattering: improved algorithms, J. Opt. Soc. Am., A 21 (2004) 606–621.
[17] T. Poon, T. Kim, Engineering Optics with Matlab, World Scientific Publishing, Singapore, 2006.
[18] B.E.A. Saleh, M.C. Teich, Fundamentals of Photonics, John Wiley & Sons, New York, 1991.
[19] Q. Sheng, H. Cheng, An adaptive grid method for degenerate semilinear quenching problems, Comput. Math. Appl. 39 (2000) 57–71.
[20] Q. Sheng, S. Guha, L. Gonzalez, Fast computer simulations of the Helmholtz equation solutions in multi-layer medians with high wavenumbers, Technical Report, AFRL/MLPJ-0804, 2006.
[21] J. Shibayama, K. Matsubara, M. Sekiguchi, J. Yamauchi, H. Nakano, Efficient nonuniform schemes for paraxial and wide-angle finite-difference beam propagation methods, J. Lightwave Technol. 17 (1999) 677–683.
[22] D. Xiu, J. Shen, An efficient spectral method for acoustic scattering from rough surfaces, Commun. Comput. Phys. 2 (2007) 54–72.